The ASC Protein Controls the Severity of Systemic AA Amyloidosis in Mice

Marco Losa[1], Patrick Schürch[2], Manfredi C. Carta[1], Itzel Condado Morales[1], Karl Frontzek[1], Veronika Lysenko[2], Asvin KK Lakkaraju[1], Mirzet Delic[1], Petra Schwarz[1], Gunilla T. Westermark[4], K. Peter Nilsson[5], Mario Nuvolone[3], Alexandre P. A. Theocharides[2], Simone Hornemann[1], Adriano Aguzzi[1,†]

[1] Institute of Neuropathology, University of Zurich, Zurich, Switzerland

[2] Department of Medical Oncology and Hematology, University Hospital Zurich, Zurich, Switzerland

[3] Amyloidosis Research and Treatment Center, Fondazione Istituto di Ricovero e Cura a Carattere Scientifico (IRCCS) Policlinico San Matteo, University of Pavia, Pavia, Italy

[4] Department of Medical Cell Biology, Uppsala University, Uppsala, Sweden

[5] Department of Physics, Chemistry and Biology, Linköping University, Linköping, Sweden

†Corresponding author:

Adriano Aguzzi

Institute of Neuropathology, University Hospital of Zurich

Schmelzbergstrasse 12, CH-8091 Zurich, Switzerland

Tel: +41-44-255-2108, E-mail: adriano.aguzzi@usz.ch

Keywords: *Pycard*, *Asc*, ASC, inflammasomes, NLRP3, innate immune system, serum amyloid A, SAA, acute-phase protein, AA amyloidosis, inflammation, macrophages, phagocytosis

Abstract word count: 209

Main text word count: 5837

Abstract

The apoptosis-associated speck-like protein containing a caspase recruitment domain (ASC) protein is a component of inflammasomes, inflammation-mediating complexes that include Nucleotide-Binding Oligomerization Domain, Leucine Rich Repeat And Pyrin Domain Containing 3 (NLRP3). ASC and NLRP3 components aggregate to form ASC specks, which can cross-seed Aβ aggregation in Alzheimer's disease (AD). Here we asked whether ASC is involved in additional protein misfolding diseases (PMDs). AA amyloidosis is a severe complication of chronic inflammatory conditions caused by the aggregation of Serum Amyloid A (SAA) protein. Since AA and Aβ aggregates share similar biochemical properties, such as β-sheet structures, we hypothesized that ASC inflammasomes may be involved in SAA/AA recruitment, aggregation, processing and removal. We therefore investigated the role of ASC in AA amyloidosis *in vivo*, employing a murine AA amyloidosis model in *Asc*-ablated mice. We show that ASC exerts a crucial role in SAA recruitment in the presence of AA fibrils, that splenic AA amyloid load was decreased in *Asc*$^{-/-}$ mice, that the presence of ASC accelerates SAA fibril formation and that ASC is important for SAA-activated phagocytosis of macrophages. We conclude that ASC modulates both SAA serum levels and the severity of AA amyloidosis in mice. ASC may represent a therapeutic target in AA as well as other amyloidosis entities.

50 **Introduction**

51 In inflammatory conditions, proinflammatory cytokines stimulate hepatocytes to release the
52 acute-phase reactant SAA into the blood stream. During the acute-phase response, the serum
53 concentration of SAA increases as much as 1000-fold from its baseline concentration (1, 2).
54 AA amyloidosis may ultimately develop when persistently high SAA serum concentrations
55 hamper proper SAA processing and clearance, leading to extracellular deposition of
56 aggregated AA fibrils and SAA recruitment to the site of amyloid. AA fibrils are predominantly
57 composed of degradation products of SAA1, an isoform of SAA, which dissociates from its
58 carrier protein high density lipoprotein (HDL) prior to its conversion to amyloid fibrils (3-9).
59 Amyloid aggregates, composed of AA fibrils and other components, are deposited in the
60 extracellular compartment of the spleen, kidney, liver and heart, which can lead to life-
61 threatening complications due to disruption of tissue integrity (10). Various types of chronic
62 inflammatory conditions, such as chronic bacterial and viral infections (e.g. tuberculosis,
63 intravenous drug abuse, hepatitis B/C), chronic inflammations (e.g. inflammatory bowel
64 diseases, rheumatic arthritis, vasculitis), hereditary mutations (e.g. familial Mediterranean
65 fever or FMF) and neoplastic diseases (e.g. lymphomas) are associated with systemic AA
66 amyloidosis (11, 12). Clinically, systemic AA amyloidosis is often asymptomatic, up to a tipping
67 point in disease progression that heralds rapid health deterioration. At manifestation, AA
68 amyloidosis patients often exhibit proteinuria and progressive kidney dysfunction, followed
69 by liver and heart failure. Current therapies have a limited impact on disease progression and
70 mortality and the exact molecular mechanisms behind the pathogenesis of AA amyloid
71 formation and SAA recruitment remain unclear to date (11, 13). To our knowledge, no
72 therapeutic approaches that directly interfere with SAA recruitment or AA amyloid formation
73 are of avail, meaning that treatment of AA amyloidosis primarily aims to reduce the underlying
74 inflammatory state.

75 However, recent insights into the field of neurodegenerative PMDs such as Alzheimer's
76 disease might also be relevant to systemic AA amyloidosis. AD is characterized by the
77 extracellular deposition of aggregates composed of misfolded amyloid β (Aβ) proteins in the
78 central nervous system. Misfolded Aβ proteins contain a larger β-sheet content than soluble
79 Aβ proteins. Similarly, amyloidogenic SAA proteins exhibit a high propensity to form AA fibrils
80 in their misfolded state, where they exhibit increased β-sheet content.

81 The innate immune system and its components, including inflammasomes, represent the first
82 line of defence to transduce immediate danger signals into a cytokine response, cell death and
83 the activation of the adaptive immune system (14). Furthermore, the innate immune system
84 is involved in the pathogenesis of PMDs (15-17). Upon activation of cytosolic pattern
85 recognition receptors (PRR) of innate immune cells, such as the NACHT-, LRR- and pyrin (PYD)-
86 domain-containing protein 3 (Nalp3) of microglia or macrophages, the adaptor protein,
87 apoptosis-associated speck-like protein containing a caspase recruitment domain (ASC) is
88 recruited, which in turn induces assembly of helical ASC fibrils (18-22). Subsequently, effector
89 caspase-1 is recruited and activated to form mature inflammasomes, enabling them to cleave
90 the proinflammatory cytokine pro-IL1β to IL-1β. ASC fibrils may ultimately transform into large
91 paranuclear ASC specks, helical fibrillary assembly of ASC proteins that can be released from
92 microglia and other tissue-resident macrophages by gasdermin D-mediated pyroptotic cell
93 death (23).
94 Inflammation and NLRP3/ASC inflammasomes play an eminent role in the pathogenesis of AD
95 (24-26). Intrahippocampal injection of microglia-derived ASC specks leads to Aβ cross-seeding
96 in APP/PS1 *Asc* wildtype (wt) mice, while cross-seeding and spreading of Aβ pathology was
97 reduced in APP/PS1 *Asc*$^{-/-}$ mice. Furthermore, stereotactic intrahippocampal co-injection of
98 ASC specks and anti-ASC antibody prevented the increase in Aβ pathology *in vitro* and *in vivo*
99 (25, 27).
100 Intriguingly, several reports point towards a role of ASC in the pathogenesis of AA amyloidosis.
101 For instance, ASC has been shown to co-localize with AA amyloid in kidney biopsies from
102 patients with AA amyloidosis secondary to the hereditary inflammatory condition FMF, where
103 a gain-of-function mutation in the *Pyrin* gene activates ASC inflammasomes and leads to
104 chronic upregulation and expression of SAA (28). Moreover, SAA activates the NLRP3
105 inflammasome of human myeloid cells via an interaction with the P2X7 receptor, which
106 induces ASC release *in vitro* through a cathepsin B-sensitive pathway (29). In line with this
107 finding, SAA (as well as lipopolysaccharide) is capable of activating murine macrophages (30).
108 A murine model of AA amyloidosis has been developed and established. In this model,
109 subcutaneous administration of silver nitrate ($AgNO_3$), coupled with an intravenous
110 application of preformed SAA fibrils (known as Amyloid Enhancing Factor or AEF), rapidly
111 induces the AA amyloidosis phenotype, with respect to splenic AA amyloid deposition (31-33).

112 $AgNO_3$ serves as a proinflammatory stimulus that leads to elevation in SAA serum levels, while
113 preformed AA fibrils serve as a template for SAA aggregation (34).
114 The involvement of the innate immune system in AA amyloidosis has been described on a
115 cellular level. For instance, depletion of splenic macrophages delays or inhibits AA amyloid
116 accumulation in mice (31, 35). Furthermore, macrophages were shown to clear AA amyloid
117 via Fc-receptor-mediated phagocytosis (36). However, a role of inflammasomes in SAA
118 recruitment and AA fibril formation has not been described to date.
119 We, therefore, sought to investigate the role of ASC in the pathogenesis of AA amyloidosis *in*
120 *vivo* and assessed the temporal development of AA amyloidosis with a focus on SAA serum
121 concentrations and splenic AA amyloid. Here, we report that *Asc* wt mice exhibited a
122 pronounced decrease in SAA serum concentration together with a concomitant increase in
123 splenic amyloid load upon AA induction. In contrast, these phenomena were attenuated in
124 the absence of ASC. Furthermore, ASC is incorporated in splenic AA amyloid and its presence
125 accelerates SAA fibril formation. In addition, *Asc*$^{-/-}$ bone marrow-derived macrophages did no
126 longer exhibit increased SAA-stimulated phagocytosis activity *in vitro*, suggesting an altered
127 macrophage processing in the absence of ASC.
128 In summary, we conclude that ASC modulates both SAA serum levels and the severity of AA
129 amyloidosis in mice and may, therefore, be a potential therapeutic target in AA amyloidosis.
130

131 **Results**

132 *Amyloid induction*

133 To investigate the role of ASC in the pathogenesis of AA amyloidosis *in vivo*, *Asc* wt and
134 *Asc*$^{-/-}$ female and male F2 generation littermates were injected with $AgNO_3$ and preformed AA
135 fibrils (amyloid-enhancing factor, AEF) for AA amyloidosis induction (AA mice), whereas
136 control mice were only injected with PBS, AEF or $AgNO_3$ (**Fig. 1a-b**). 79 mice were included in
137 this study and AA was induced in 22 *Asc* wt and 24 *Asc*$^{-/-}$ mice. A total of 33 mice were only
138 injected with either PBS, $AgNO_3$ or AEF and served as controls (**Table S1**). The experimental
139 overview including injection schematic, blood withdrawals and euthanasia regimen is
140 illustrated in **Fig. 1b**. To assess AA amyloid deposition over time, mice were sacrificed either
141 at day 16 or at day 30, two days after the last $AgNO_3$ injection. The presence of amyloid in
142 spleens was assessed by staining histological sections of paraffin-embedded tissue with Congo
143 red, upon which we saw the characteristic apple-green birefringence under polarized light
144 (**Fig. S1**). No amyloid could be detected in control group mice that were only injected with
145 either PBS, $AgNO_3$ or AEF. The detailed characteristics of the experimental groups are
146 summarized in **Table S1**. Age distribution did not differ significantly between experimental
147 groups (**Table S2**).

148

149 *The recruitment of Serum Amyloid A in AA amyloidosis is modulated by ASC*

150 The development of AA amyloidosis is a consequence of excessive production and recruitment
151 of SAA. We, therefore, assessed SAA serum levels in *Asc* wt and *Asc*$^{-/-}$ mice by enzyme-linked
152 immunosorbent assay (ELISA) at baseline (before any injection) as well as at 9, 24, 48, 72- and
153 96-hours post injection (hpi) of $AgNO_3$ and AEF (**Fig. 1b and Fig. 2).** At baseline and at 9 hpi,
154 there was no difference between mean SAA serum concentrations of all experimental *Asc* wt
155 and *Asc*$^{-/-}$ groups. However, at 24 hpi, the timepoint at which we expected serum acute-phase
156 proteins to peak (1, 37), we observed differences in SAA serum levels between experimental
157 groups, depending on *Asc* genotype and the presence or absence of AEF. SAA serum levels of
158 *Asc* wt mice only treated with $AgNO_3$ were significantly higher than in *Asc* wt mice with
159 $AgNO_3$+AEF ($p=0.0348$), suggesting that SAA is recruited in the presence of preformed AA
160 fibrils and therefore decreased in serum. Furthermore, the decrease in SAA serum
161 concentration observed in *Asc* wt AA mice, was abrogated in *Asc*$^{-/-}$ AA mice ($p=0.0035$). Mean

162 SAA serum concentrations of *Asc*$^{-/-}$ AA mice were slightly higher than the SAA serum
163 concentration of the $AgNO_3$-only injected *Asc*$^{-/-}$ groups at 9, 24, 48 and 72 hpi (p=0.0604 at 72
164 hpi), possibly because the ELISA detected injected preformed AA fibrils that were still present
165 in the blood stream (**Fig. S2**).
166 As presumed, 48 hours after injection, SAA serum concentrations decreased in all
167 experimental groups. However, at this time point the difference between *Asc* wt and *Asc*$^{-/-}$ AA
168 mice was still significant (p=0.0048). Depending on the genotype, the difference between SAA
169 serum concentrations of the two *Asc* wt and *Asc*$^{-/-}$ AA induced groups persisted up to 72 hours
170 after injections (p=0.034).
171 Finally, 96 hours after injection there was no longer any significant difference in SAA serum
172 concentration. Overall, *Asc*$^{-/-}$ AA mice were found to have the highest SAA serum
173 concentration among all experimental groups. Based on these results, we postulate that in
174 experimental amyloidosis, ASC facilitates the recruitment and deposition of SAA in murine AA
175 amyloidosis. Detailed SAA serum values are given in **Table S3**.
176
177 *$AgNO_3$-induced acute-phase responses in Asc*$^{-/-}$ *and wildtype mice*
178 While it is known that aluminum-containing adjuvants activate the NLRP3 inflammasome (38),
179 it is not known whether $AgNO_3$ stimulates ASC-dependent inflammasome pathways of innate
180 immune cells. To investigate this question, we assessed SAA levels of $AgNO_3$-only injected *Asc*
181 wt and *Asc*$^{-/-}$ mice by ELISA and compared their SAA serum concentrations at baseline and up
182 to 96 hours after injection (**Fig. 1b and Fig. 2**).
183 As mentioned previously serum concentrations of SAA and other acute-phase proteins peak
184 at around 24 hours after a proinflammatory stimulus. At this time, *Asc* genotype did not
185 significantly impact SAA serum levels after $AgNO_3$ stimulation, as there was no significant
186 difference in SAA serum concentration between *Asc* wt and *Asc*$^{-/-}$ mice that had only been
187 treated with $AgNO_3$. The same was also true for all successive timepoints. Genetic ablation of
188 *Asc* did not significantly impact $AgNO_3$-induced SAA levels, suggesting that ASC-dependent
189 inflammasomes do not significantly contribute to $AgNO_3$ sensing. Given that the experimental
190 AA amyloidosis model requires an $AgNO_3$ treatment to induce inflammation, we conclude that
191 applying the murine AA amyloidosis model to *Asc*$^{-/-}$ mice would allow us to study the role of
192 ASC in SAA recruitment and AA amyloid formation.

193

194 *Decreased splenic amyloid deposition in the absence of ASC-dependent inflammasomes*

195 In mice with experimental AA amyloidosis, we observed that amyloid deposition commenced
196 in the marginal zone of the white pulp, followed by red pulp invasion, which is in accordance
197 with other studies (31-33). To assess amyloid load, we stained spleen sections with the
198 luminescent conjugated polythiophene (LCP) HS-310. Representative spleen sections of *Asc*
199 wt and *Asc*$^{-/-}$ AA mice are shown in **Fig. 3a-d**. Overall, *Asc* wt mice exhibited more pronounced
200 red pulp invasion of amyloid compared to *Asc*$^{-/-}$ mice (white arrows). In the PBS-only, AEF-only
201 and $AgNO_3$-only treated control mice, no amyloid could be detected (**Fig. S1 and Fig. S3**). To
202 quantify the amyloid load of AA mice, we calculated, based on fluorescence, the integrated
203 density, which is the sum of the values of the pixels in the region of interest and the
204 percentage of the amyloid area deposited within spleen sections (HS-310+). The mean
205 fluorescence integrated density (A.U./μm^2) differed significantly between *Asc* wt AA mice of
206 the 16-days and the 30-days group (p=0.0035), whereas it did not in *Asc*$^{-/-}$ AA mice (**Fig. 3e**).
207 In addition, there was a significant difference in amyloid load between *Asc* wt and *Asc*$^{-/-}$ mice
208 of the 30-days group (p=0.0242). Similar results were seen in the analysis of the amyloid area
209 deposited in the spleen. There was a significant increase in amyloid from day 16 to day 30 in
210 *Asc* wt AA mice (p=0.0004), whereas the increase of amyloid *Asc*$^{-/-}$ AA mice was attenuated
211 and not significant within the same period. Furthermore, *Asc*$^{-/-}$ AA mice from the 30-days
212 group revealed a decreased amyloid deposition compared to *Asc* wt AA mice (p=0.0125) (**Fig.
213 3f**). Detailed area values are given in **Table S4**. Using Western Blot (WB), we assessed the
214 presence and quantity of SAA in spleen homogenate of four *Asc* wt and five *Asc*$^{-/-}$ AA mice with
215 the highest splenic amyloid load, as assessed by LCP staining (**Fig. 3g-h**). In WB we detected
216 bands with sizes below 12 kDa, which probably represented proteolytic degradation products
217 of AA amyloid (39). Moreover, ASC was found to be highly expressed, adjacent and integrated
218 to amyloid deposits throughout the spleen of *Asc* wt AA mice (**Fig. 4a**). In summary, these data
219 suggest that AA amyloid load and deposition depend on *Asc* genotype.

220

221 *Accelerated SAA fibrillation in presence of ASC*

222 In order to assess the effect of ASC on SAA fibril formation we performed an *in vitro* SAA
223 aggregation assay in presence as well as in absence of ASC specks (**Fig. 4b**). The halftime ($t_{1/2}$),

224 where the relative aggregation concentration is 0.5, was significantly reduced in presence of
225 ASC specks and inversely correlated with increased concentrations. The $t_{1/2}$ of murine SAA
226 aggregation was significantly reduced in presence of 100k ASC specks compared to the
227 samples that only contained murine SAA (p=0.0282). Furthermore, in presence of 200k and
228 500k ASC specks the lag phase was further reduced significantly, respectively (p=0.0075,
229 p<0.0001) (**Fig. 4c**). Hence, this suggests that the presence of the ASC protein accelerates SAA
230 fibril formation. Detailed values are given in (**Table S5**).
231
232 *Splenic architecture and peripheral blood in AA amyloidosis*
233 Prolonged elevation of serum SAA is required to trigger AA amyloidosis (5). Once present, AA
234 aggregates progressively disrupt tissue integrity and ultimately impair physiological function
235 of affected organs. Furthermore, patients with systemic AA amyloidosis may also exhibit
236 altered red blood cell and platelet volumes according to recent reports (40, 41). Moreover,
237 the presence of platelets in the circulation and platelet-derived enhancing factors supply
238 inflammasome activation and boost inflammasome capacity of macrophages, neutrophils and
239 monocytes in inflammation (42). Since SAA activates the NLRP3 inflammasome of innate
240 immune cells, as described above, we assessed the cellular composition of the spleen and of
241 peripheral blood at baseline and after induction of experimental AA amyloidosis, in *Asc* wt and
242 *Asc*$^{-/-}$ mice. We assessed B cells, T cells, dendritic cells, neutrophils as well as macrophages
243 including M1- and M2-like macrophages in the spleen (**Fig. S4**). Altogether, mice that had only
244 been treated with $AgNO_3$ as well as mice with AA induction had an increased splenic
245 macrophage infiltration compared to baseline state, underscoring the involvement of innate
246 immune cells in AA amyloidosis. Macrophage infiltration was neither dominated by M1- nor
247 by M2-like macrophages (**Fig. S4c**). Furthermore, we assessed the transcriptional state of
248 splenic macrophages from *Asc* wt and *Asc*$^{-/-}$ AA mice by RNA sequencing (**Fig. S5**). Significant
249 (p<0.05 and fdr<0.01) transcriptional changes between specimen were mainly found in the
250 *Asc* gene (**Fig. S5c and Fig. S5d**). Lymphocyte, monocyte, granulocyte, red blood cell and
251 platelet counts were additionally assessed in peripheral blood (**Fig. S7 and Fig. S8**).
252 Interestingly, platelet count at baseline was higher in *Asc*$^{-/-}$ compared to *Asc* wt mice
253 (p=0.0172). The same accounted for *Asc*$^{-/-}$ AA mice from the 30-days group (p=0.0357) (**Fig.
254 S7**).

255

256 *Impaired phagocytic activity of SAA-activated Asc$^{-/-}$ bone marrow-derived macrophages*

257 Macrophages and monocytes play a central role in AA amyloidosis. First, monocytes are
258 sufficient to transfer AA amyloidosis *in vivo* (43). Furthermore, macrophages co-localize with
259 AA amyloid in the spleen of AA mice (32). Moreover, phagocyte depletion delays or inhibits
260 AA amyloid accumulation (31, 35). Another important fact is that AA amyloid undergoes Fc-
261 receptor-mediated phagocytosis by macrophages, which is initiated by host-specific
262 antibodies that target AA protein (36). Given the importance of monocytes and macrophages
263 in AA amyloidosis, that SAA activates macrophages (29, 30) and that *Asc* heterozygous
264 astrocytes have an increased Aβ phagocytosis in AD mice (44), we sought to test whether ASC
265 may modulate the phagocytic activity of *Asc* wt and *Asc*$^{-/-}$ murine BMDMs *in vitro* (**Fig. S6a-b**).
266 We, therefore, exposed SAA-activated and non-(SAA)-activated murine BMDMs to an *in vitro*
267 phagocytosis assay (**Fig. S6c**). There was no significant difference in phagocytic activity
268 between unstimulated BMDMs of both *Asc* genotypes. The highest phagocytic activity among
269 the murine BMDMs was seen in SAA-activated *Asc* wt BMDMs as compared to non-stimulated
270 *Asc* wt BMDMs (p=0.0015). Compared to their wildtype counterparts, we observed lower
271 phagocytic activity in SAA-activated *Asc*$^{-/-}$ BMDMs. Furthermore, there was a difference in
272 phagocytic activity between SAA-stimulated *Asc* wt and *Asc*$^{-/-}$ BMDMs (p=0.0002). Hence, the
273 *Asc* genotype indeed affects the phagocytosis of SAA-activated BMDMs. Nevertheless, the
274 absence of SAA-induced phagocytosis stimulation in *Asc*$^{-/-}$ BMDMs (compared to *Asc* wt
275 BMDMs) supports the fact that the ASC protein is crucial for the decreased AA amyloid
276 deposition in *Asc*$^{-/-}$ mice rather than the altered phagocytosis in absence of ASC *per se*.
277 Detailed values are given in (**Table S6**).

278 **Discussion**

279 Protein misfolding diseases and their associated degenerative disorders display a major
280 socioeconomic burden worldwide and scarcity of specific therapies still prevails.

281 In the present study we investigated the role of ASC in the pathogenesis of systemic AA
282 amyloidosis *in vivo.* To do so, we harnessed an experimental platform of AA amyloidosis and
283 employed mice in which *Asc*, the gene coding for the central component of the NLRP3
284 inflammasome, had been ablated (45). We report that ASC modulates SAA serum levels and
285 controls the severity of murine AA amyloidosis. Given its potential to influence amyloid
286 formation, ASC may represent a valid therapeutic target for the treatment of AA amyloidosis.

287 A fundamental role of the innate immune system is the sensing of environmental danger
288 signals, which is mediated by the family of cytosolic pattern recognition receptors (PRR).
289 Nalp3, the receptor of the NLRP3 inflammasome, is a PRR that mediates the
290 immunostimulatory properties of aluminum containing adjuvants (38). Therefore, we began
291 by assessing whether silver nitrate ($AgNO_3$), the proinflammatory stimulus required to trigger
292 murine AA amyloidosis in this study, is sensed by ASC-dependent inflammasomes and whether
293 $AgNO_3$ injection leads to a similar increase in SAA serum concentrations in *Asc*$^{-/-}$ and *Asc* wt
294 mice. $AgNO_3$-only injected *Asc*$^{-/-}$ mice showed mean SAA serum elevations that were
295 comparable to those in *Asc* wt mice that had received the same treatment. We conclude that
296 ASC inflammasomes do not play a major role in silver nitrate sensing and that the murine AA
297 amyloidosis model was suitable for our *in vivo* study in *Asc*$^{-/-}$ animals.

298 In order to determine the role of ASC in SAA kinetics upon an inflammatory stimulus, we
299 assessed the temporal development of SAA serum concentrations of *Asc* wt and
300 *Asc*$^{-/-}$ experimental mice. Peak SAA concentration was reached 24 hours after injection; at this
301 timepoint SAA serum levels of *Asc* wt mice with experimental AA amyloidosis were
302 significantly decreased, compared to *Asc* wt mice that had solely been treated with $AgNO_3$ (no
303 AEF). Intriguingly, in the presence of injected preformed AA fibrils (AEF) but absence of
304 endogenous ASC, serum SAA concentrations of *Asc*$^{-/-}$ mice remained increased up to 72 hours
305 post injections. These data suggest that ASC may serve as an enhancing factor for the
306 aggregation of SAA and AA templated by preformed AA fibrils. SAA levels only decreased in
307 the presence of ASC, suggesting that ASC may mediate a SAA serum-to-tissue or serum-to-cell
308 translocation.

309 We then checked for the presence of amyloid after AA induction using Congo red and LCP
310 stains in all experimental groups. We found that only mice who had undergone the full
311 experimental AA amyloidosis induction protocol with $AgNO_3$ and AEF injections, but none of
312 the control mice, showed amyloid deposition.
313 ASC speck co-localization with Aβ plaques occurs in AD brains (25). Furthermore, there is
314 evidence that ASC co-localizes with AA amyloid in kidney biopsies from FMF patients suffering
315 from AA amyloidosis (28). If ASC has a propensity to bind amyloids generically, it may form
316 complexes with AA amyloid as well. Indeed, we detected the presence of ASC within AA
317 amyloid deposits in spleen tissue from *Asc* wt AA mice. In presence of ASC, the deposition of
318 AA amyloid appeared to be more invasive into the red pulp than *Asc*$^{-/-}$ AA mice, where amyloid
319 was mainly found in proximity to vessels and limited to the marginal zones of follicles.
320 Furthermore, the presence of ASC specks facilitated and accelerated SAA fibril formation *in*
321 *vitro*, which supports the idea that ASC inflammasome protein assemblies serve as a generic
322 protein aggregation-enhancing platform in various central and peripheral PMDs where the
323 innate immune system is involved. It has recently been reported that there are few ASC specks
324 in fully matured lymphoid organs, which might explain their rather sparse distribution in the
325 examined tissues (46). However, amyloid was significantly reduced in *Asc*$^{-/-}$ compared to *Asc*
326 wt mice after 30 days of inflammation. AA amyloid consists of multiple components such as
327 serum amyloid P, proteoglycans, glycosaminoglycans, lipid rafts as well as SAA (47, 48).
328 Although SAA displayed a non-significant difference in western blot analysis, the ASC protein
329 incorporation into amyloid of *Asc* wt mice with AA as well as the compelling amyloid load
330 reduction in *Asc*-ablated mice with AA (as visible in LCP-stained tissue) strongly advocate ASC
331 as the driving force in the pathogenesis of AA amyloidosis. SAA western blot analysis of spleen
332 homogenate from AA mice revealed multiple bands running between 8 and 12 kDa in size.
333 Murine SAA has a mass of approximately 11.8 kDa. The bands <12 kDa in size most likely
334 represent proteolytic degradation products of AA amyloid (39, 49).
335 It is widely recognized that macrophages co-localize with amyloid deposits and that Fc-
336 receptor-mediated phagocytosis plays an important role in deposition, processing and
337 clearing of AA amyloid (31, 32, 36, 39, 50). We, therefore, tested another experimental
338 paradigm, where we aimed to elucidate the role of ASC in the phagocytic activity of
339 macrophages. Interestingly, *Asc*$^{+/-}$, but not *Asc*$^{-/-}$, astrocytes exhibit increased phagocytosis of

340 Aβ in a mouse model of AD (44). Moreover, macrophages and monocytes are capable of
341 converting endocytosed SAA to processed extracellular AA amyloid *in vitro* (51, 52). We,
342 therefore, investigated whether *Asc*$^{-/-}$ macrophages reveal enhanced phagocytic activity, as
343 this might be contributory to altered and less AA amyloid deposition or AA processing. We
344 observed that SAA-stimulated *Asc* wt murine BMDMs showed increased phagocytosis,
345 compared to *Asc*$^{-/-}$ macrophages. These findings suggest that the reduced splenic AA amyloid
346 in *Asc*$^{-/-}$ mice load is mainly due to the absence of ASC and not due to enhanced phagocytosis
347 of *Asc*$^{-/-}$ BMDMs. In addition, transcriptomic analysis of splenic macrophages of AA diseased
348 mice revealed mainly *Asc* gene upregulation among wildtype specimen. These data further
349 underline the crucial role of ASC in AA amyloidosis. Nonetheless, an impaired phagocytosis of
350 SAA-activated *Asc*$^{-/-}$ macrophages might potentially contribute to altered AA processing and
351 removal.
352 Finally, we investigated whether splenic and peripheral blood cellular alterations occurred in
353 *Asc* wt and *Asc*$^{-/-}$ AA mice. We assessed splenic cellular composition with a focus on B cells, T
354 cells, dendritic cells, neutrophils and macrophages (including M1- and M2-like polarized
355 macrophages), together with peripheral blood composition of lymphocytes, monocytes,
356 granulocytes, red blood cells and platelets. There was an increased splenic macrophage
357 infiltration in $AgNO_3$-only and AA induced mice at day 16 and 30, compared to baseline levels,
358 which underscores the involvement of innate immune cells in the pathogenesis of AA
359 amyloidosis.
360 When comparing peripheral blood composition of *Asc* wt to *Asc*$^{-/-}$ mice, we observed a slightly
361 increased baseline platelet count of *Asc*$^{-/-}$ mice as well as marginally increased platelets
362 numbers in *Asc*$^{-/-}$ AA mice at day 30 in peripheral blood. According to a recent report, platelets
363 release enhancing factors that boost the inflammasome activation of innate immune cells
364 (42). We speculate that in the absence of ASC, platelets might be increased as part of a
365 compensatory mechanism.
366 In summary, we conclude that ASC modulates SAA serum levels, accelerates SAA fibril
367 formation and controls the severity of AA amyloidosis. Although we have identified ASC as a
368 critical protein in the pathogenesis of AA amyloidosis, additional work may be required to
369 resolve the precise molecular mechanism of its involvement. It is conceivable that the
370 modulatory effect is not only a result of the binding properties of ASC and ASC specks for β-

371 sheet rich proteins. However, the findings of this study highlight a crucial role of ASC in SAA
372 recruitment and amyloid deposition in AA amyloidosis, which might also be relevant in the
373 pathogenesis of further systemic amyloidoses. It may very well be that ASC and its protein
374 assemblies serves as aggregation enhancing platform in various PMDs. Finally, it is possible
375 that our findings might have therapeutic implications, since ASC could be a target of disease-
376 modifying therapies that aim to reduce amyloid deposition in various PMDs.

377 **Material and Methods**

378

379 Mice

380 Animal care and experimental protocols were in accordance with the Swiss Animal Protection
381 Law and approved by the Veterinary office of the Canton of Zurich (permit ZH131-16). Mice
382 were bred in a high hygienic grade facility of the University Hospital of Zurich (BZL) and housed
383 in groups of 2-5. Mice were under a 12 hours light/ 12 hours dark cycle (from 7 a.m. to 7 p.m.)
384 at 21 ± 1°C. *Asc*-deficient mice (B6.129-*Pycard*^{tm1Vmd}) were generated as previously published
385 in (45). C57BL/6 wildtype mice were obtained from the Jackson laboratory. To minimize
386 environmental bias and potential differences in microbiota, F2 littermates were bred. We
387 perfomed the experiments with highest possible gender and age congruence among
388 experimental groups (**Table S1-S2**). Mice were randomly assigned to the experiments.

389

390 Genotype screening

391 Ear biopsies were digestd and subjected to PCR. An 859 bp *Asc* allele fragment was amplified
392 using forward 5'-GAAGCTGCTGACAGTGCAAC-3' and reverse 5'-CTCCAGGTCCATCACCAAGT-3'
393 primers. Amplification of a 275 bp gDNA fragment from the B6.129-*Pycard*^{tm1Vmd} Neo cassette
394 was done using forward 5'-TGGGACCAACAGACAATCGG-3' and reverse 5'-
395 TGGATACTTTCTCGGCAGGAGC-3' primers. PCR products were run on a 1.5% agarose gel and
396 developed for genotype definition.

397

398 AA induction, injections and reagents

399 Silver nitrate (Merck) was eluted in nuclease-free water (Ambion®). AEF was prepared as
400 previously described in (53) and pH was adjusted to 7.4 before administration. AA amyloidosis
401 induction performed by injections of 100 µl AEF (i.v.) and 200 µl sterile-filtered 1 % silver
402 nitrate solution (s.c.). Repeated injections of silver nitrate were in accordance to (39) (**Fig. 1**).

403

404 Mouse serum amyloid A (SAA) measurements

405 To determine the SAA levels in mice serum, blood was withdrawn into BD Microtainer® SST™
406 Tubes at baseline and up to 96 hours post injection. Samples were left at room temperature
407 (RT) for 30 min and subjected to centrifugation at 10'000xg for 8 min at 4°C. Sample sera were
408 then transferred and stored at -80°C. SAA levels were assessed by a mouse SAA enzyme-linked
409 immunosorbent assay (ELISA) kit (abcam) according the manufacturers' guidelines. Mouse
410 serum samples were analyzed in technical triplicates. ELISA plate was developed using of 450
411 nm for absorbance.

412

413 Euthanasia and organ harvesting

414 Upon euthanasia, organs were harvested and kept on ice in Iscove's Modified Dulbecco's
415 Medium (IMDM) (ThermoFisher Scientific) until measurement and further usage (no longer
416 than 4 hours). Bone marrow cells of tibia, femur and pelvis were flushed into IMDM using 25G
417 needles (B. Braun). Tissue was fixated in formalin for paraffin embedding or put in Tissue-Tek®
418 O.C.T.™ compound (Sakura®) for frozen sections.

419

420 Histology and immunohistochemistry

421 Formalin-fixed and paraffin-embedded spleen sections (2-4 µm) were de-paraffinized with
422 three cycles of xylene treatment followed by re-hydration with 100 % EtOH, 96 % EtOH, 70 %
423 EtOH and water (each cycle 5 min) respectively. Hematoxylin and eosin (HE) as well as Congo
424 red (CR) staining and ASC immunohistochemistry (IHC) were performed according to standard
425 procedures used at our institute. IHC was performed with anti-ASC pAb (clone AL177,
426 AdipoGen) at a dilution of 1:500. Slides were incubated with HS-310 for 30 min at RT in the
427 dark at a final concentration of 0.3 µg/ml in PBS (54, 55). After washing, slides were mounted
428 with fluorescence mounting medium (Dako) and proceeded to fluorescence microscopy for
429 imaging (OLYMPUS BX61 fluorescence microscope system harnessing an OLYMPUS XM10
430 camera). The hexameric LCP HS-310 was produced as previously described (56).

431

432 Fluorescence and polarized microscopy

433 To analyze LCP-stained tissue sections, we assessed three different and independent visual
434 fields at 4x magnification and slides per mouse and organ. Two parameters, HS-310 positive
435 area (% of area) as well as the fluorescence integrated density (A.U./μm^2) of HS-310 were
436 calculated with the free software application ImageJ (imagej.net). To confirm the presence of
437 amyloid, we assessed the apple-green birefringence of amyloid under polarizing light in Congo
438 red stained spleen tissue sections (**Fig. S2**). FACS sorted splenic macrophages were visually
439 confirmed by filter settings that allowed the detection of PE-Cy5 and APC-Cy7.

440

441 Immunoblot analysis

442 To determine SAA presence by WB, spleen tissues from AA induced mice were homogenized
443 in 1:9 volumes (w/v) of RIPA buffer (50 mM Tris pH 7.4, 1 % NP-40, 0.25% Deoxycholic acid
444 sodium salt, 150 nM NaCl, 1 mM EGTA, protease inhibitors (complete Mini, Roche)) using
445 TissueLyser LT for 45 seconds for four cycles. Samples were cooled on ice between cycles.
446 Supernatant was transferred into new tubes after full speed centrifugation for 10 min at 4°C.
447 10 µl spleen homogenate was boiled at 95°C for 10 min with a final concentration of 1 µM DTT
448 and 4x NuPage™ LDS sample buffer (ThermoFisher Scientific). Spleen homogenate was
449 separated using SDS-PAGE (Novex NuPAGE 4-12 % Bis-Tris Gels, Invitrogen) and transferred to
450 a PVDF membrane (ThermoFisher Scientific) at 20 V for 7 min. Membrane was blocked with
451 5% milk in TBS-T (Tris-Buffered Saline, 0.1 % TWEEN®20, pH 7.6) for 3 hours at RT. Primary
452 rabbit anti-SAA antibody was overnight (o/n) incubated at 4°C at a concentration of 2.5 µg/ml
453 (**Table S7**). After 4 cycles of washing, membranes were incubated with secondary horseradish
454 peroxidase (HRP)-conjugated goat anti-rabbit IgG (H+L) (Jackson Immuno) diluted 1:5000 in
455 blocking buffer for 1 hour at RT. Blots were developed harnessing Luminata Crescendo
456 Western HRP substrate (Milipore) and visualized with the Stella system (model 3200, Raytest).
457 Actin served as loading control. Membranes were sequentially incubated with primary mouse
458 anti-actin antibody (Merck) at 1:8000 in blocking buffer at 4°C o/n. After washing membranes
459 were incubated with secondary horseradish peroxidase (HRP)-conjugated goat anti-mouse IgG

460 (H+L) (Jackson Immuno) diluted 1:8000 in blocking buffer for 1 hour at RT. Blots were
461 developed as described above (**Fig. S9**). WB quantification was performed using the free
462 software Image Studio™ Lite (licor.com).
463

464 *In vitro* SAA fibril formation

465 Recombinant murine SAA1 was generated as previously described in (57). The *in vitro*
466 aggregation assay was carried out in a black 96-well plate (Greiner Bio-One, PS, F-bottom,
467 black) on a FLUOstar OMEGA plate reader (BMG Labtech). SAA1 was dissolved in water at a
468 stock solution concentration of 10 mg/ml. The final reaction volume was 100 µl per well and
469 consisted of 50 µM murine SAA1, 20 µM Thioflavin T (abcam) and 10 mM Tris buffer pH 8.0.
470 ASC specks were recombinantly produced as previously described (58), diluted in PBS and
471 added at various concentrations. The plate was agitated every 20 min by orbital shaking for
472 10 s at 100 rpm. The assay was performed at 37°C. Fluorescence (Ex: 450nm, Em: 490 nm) was
473 measured over the course of 140 hours. Data was normalized using the free software
474 application AmyloFit according to the developers' guidelines (59).

475

476 Differentiation of bone marrow cells to bone marrow derived macrophages (BMDMs)

477 BMDMs were generated, with slight modifications, as previously published (60). BM cells were
478 harvested from tibia and femur, washed twice in PBS and resuspended in differentiation
479 medium I-10 + M-CSF (i.e. IMDM, 10 % FBS, 1 mg/ml Pen/Strep containing 25 ng/ml
480 recombinant murine M-CSF (PeproTech)) at a density of 1-2 Mio. cells/ ml. After incubation
481 for four days at 37°C differentiation medium was exchanged. On day 8 attached BMDMs were
482 detached using Accutase® (Innovative Cell Technologies, Inc.), washed twice in PBS, counted
483 and proceeded to the phagocytosis assay.
484

485 *In vitro* phagocytosis

486 The phagocytosis of BMDMs was performed using a phagocytosis assay kit (abcam). Individual
487 samples were prepared in duplicates. The in *vitro* assay was performed in 96-well tissue

488 culture plates (TPP). *Asc* wt and *Asc*$^{-/-}$ BMDMs were suspended at a density of 500'000
489 cells/ml. BMDMs were stimulated, with slight modifications, as previously published (30).
490 BMDMs were stimulated with murine SAA1 at a concentration of 2 µg/ml for 16 hours at 37°C
491 prior to phagocytosis substrate encounter. After 1-hour phagocytosis substrate incubation at
492 37°C, cells were treated according to the manufacturers' guidelines and proceeded to EnVision
493 Multimode Plate Reader (PerkinElmer) for data acquisition. The absorbance was determined
494 at 405 nm.

495

496 Assessment of cellular spleen architecture by flow cytometry

497 After sacrifice, cells were isolated from spleens using a 70 µm cell strainer (Falcon®). Following
498 red blood cell lysis cells were stained and with the following monoclonal antibodies to
499 determine cellular architecture of most abundant spleen and immune cells (**Table S8**): anti-
500 mouse CD45.2 (Biolegend), anti-mouse Gr-1 (eBioscience), anti-mouse F4/80 (eBioscience),
501 anti-mouse CD11b (Biolgegend), anti-mouse B220 (Biolegend), anti-mouse CD3 (Biolgend),
502 anti-mouse CD206 (Biolegend), anti-mouse MHCII (Biolegend) and anti-mouse CD11b
503 (eBioscience). Data acquisition and analysis was performed on a BD LSRIIFortessa™ flow
504 cytometer and FlowJo v10.6.1, respectively. Gating strategy was applied, with slight
505 modifications, as previously published (61-63).

506

507 RNA extraction and high throughput sequencing (NGS)

508 Upon FACS sorting of F4/80+/CD11b+ splenic macrophages originating from AA mice (see
509 above) total RNA was extracted using TRIzol™ Reagent (ThermoFisher Scientific) according to
510 the manufacturers' guidelines and proceeded to high throughput sequencing (NGS). RNA
511 integrity and quantity were assessed by RNA ScreenTape Analysis (Agilent). The SMARTer
512 Stranded Total RNA-Seq Kit- Pico Input Mammalian (Takara) together with a NovaSeq platform
513 (Illumina) was applied for transcriptomic data acquisition. Data was analyzed using established
514 analysis pipelines at the Functional Genomics Center Zurich (FGCZ).

515

516 Assessment of complete blood count (CBC) from peripheral blood

517 Blood was withdrawn into Microvette® 100 K3E (SARSTEDT Germany) cuvettes according to
518 the manufacturers' guidelines. To assess CBCs, samples were run on an ADVIA (Siemens
519 Healthineers) hematology system.

520

521 Statistical analysis

522 Statistical analysis was performed using Graph Pad Prism v8.0.0. If not indicated otherwise,
523 unpaired, two-tailed Student's t-tests or one-/two-way ANOVA were performed, followed by
524 post hoc analysis wherever appropriate. Statistical details are described in the respective
525 figures. A two-tailed *p*-value <0.05 was considered as statistically significant. Confidence
526 intervals were calculated at a confidence level of 95 %.

527

528 Acknowledgments

529 We thank Rita Moos, Paulina Pawlak and Prof. Dr. Michael Heneka for advice and expertise.
530 We appreciate that Dr. Emmanuel Contassot shared the B6.129-*Pycard*^{tm1Vmd} mice. We thank
531 Dr. Marcus Fändrich and his colleagues for providing murine SAA1 protein. A.P.A.T. is
532 supported by the Professor Dr. Max Cloëtta Foundation. AA is the recipient of an Advanced
533 Grant of the European Research Council, the Swiss National Foundation, and the Nomis
534 Foundation.

535

536 Statement of author contribution

537 Conceived and designed the experiments: ML, AA. Performed the experiments: ML, PS, VL,
538 ICM, MC, MD. Analyzed the data: ML, PS. Contributed reagents and materials: KF, AKKL, GTW,
539 KPRN, MN, SH. Wrote the manuscript: ML. Edited manuscript: all authors.

540

Declaration of interests

The authors declare no competing interests.

543 **Main figures**

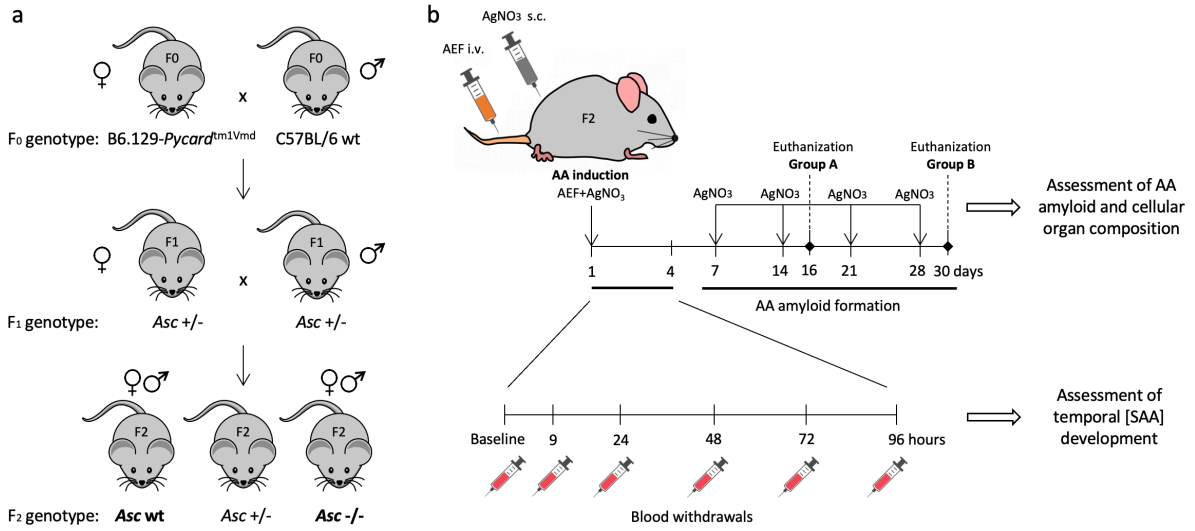

544

545 Figure 1.

546 **Experimental overview.**

547 **(a)** Mouse schematic depicting breeding strategy. B6.129-*Pycard*^{tm1Vmd} (*Asc* is also known as
548 *Pycard*) were crossed with C57BL/6 mice. *Asc* heterozygous F1 progenies were mated to
549 generate *Asc* wt and *Asc*$^{-/-}$ F2 generation littermates. **(b)** Experimental set-up. AA was induced
550 by intravenous (i.v.) injection of amyloid enhancing factor (AEF) and subcutaneous (s.c.)
551 injection of silver nitrate ($AgNO_3$). To assess SAA serum concentration development in a
552 temporal manner, blood was withdrawn at indicated time points. Repeated $AgNO_3$ injections
553 were performed with an interval of 7 days. Group A (16 days in experiment) received two,
554 whereas group B (30 days in experiment) received four additional $AgNO_3$ injections after AA
555 induction. Group A and B mice were euthanized two days after the last silver nitrate injection,
556 either on day 16 or day 30, respectively. Organs of interest were harvested and processed for
557 further analysis.

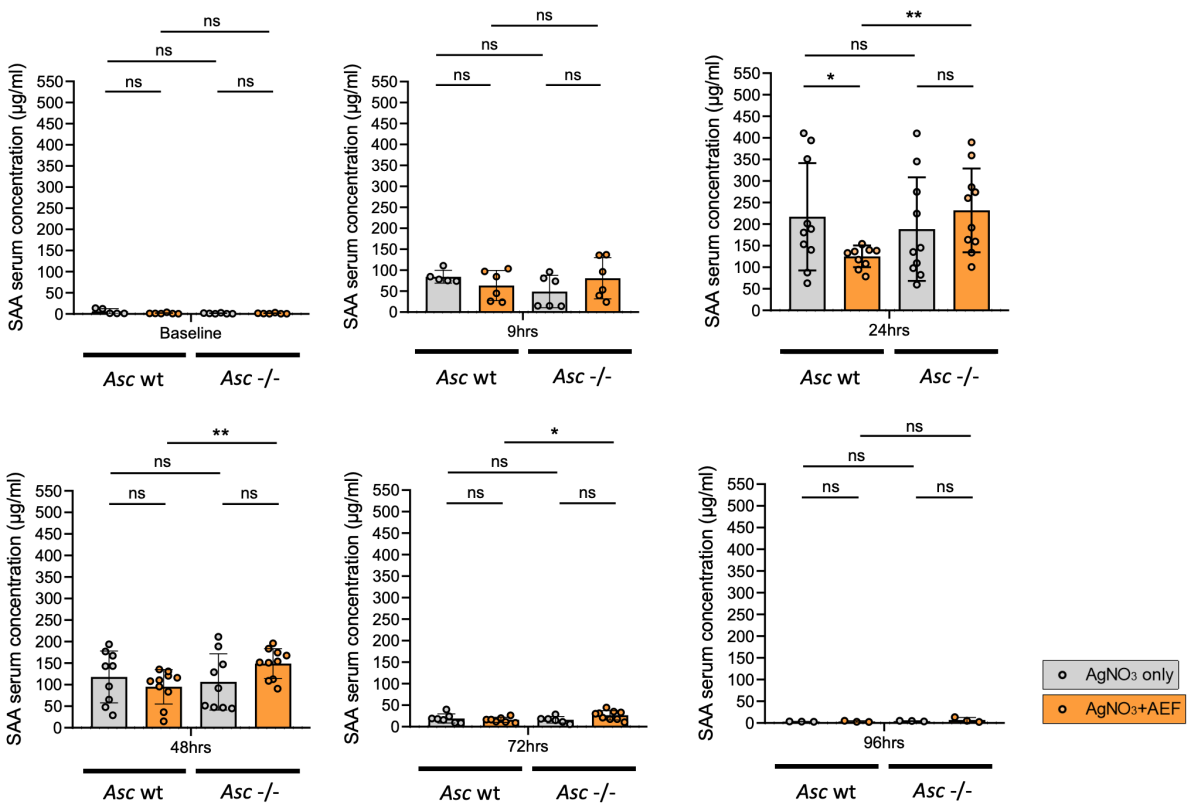

558

559 Figure 2.

560 **The recruitment of serum amyloid A in AA amyloidosis is modulated by ASC.**

561 Scatter plots depicting SAA serum concentrations in *Asc* wt and *Asc*$^{-/-}$ mice in a temporal
562 manner, from baseline up to 96 hours after injection of either $AgNO_3$ only (grey bars) or
563 $AgNO_3$+AEF (orange bars) **(a-f)**. Each dot at a given timepoint represents an individual animal.
564 SAA serum measurements were performed in technical triplicates. Results are represented as
565 mean ± standard deviation (error bars). ** $p<0.01$, * $p<0.05$, ns; not significant. Analysis was
566 performed using unpaired two-tailed Student's t-tests.

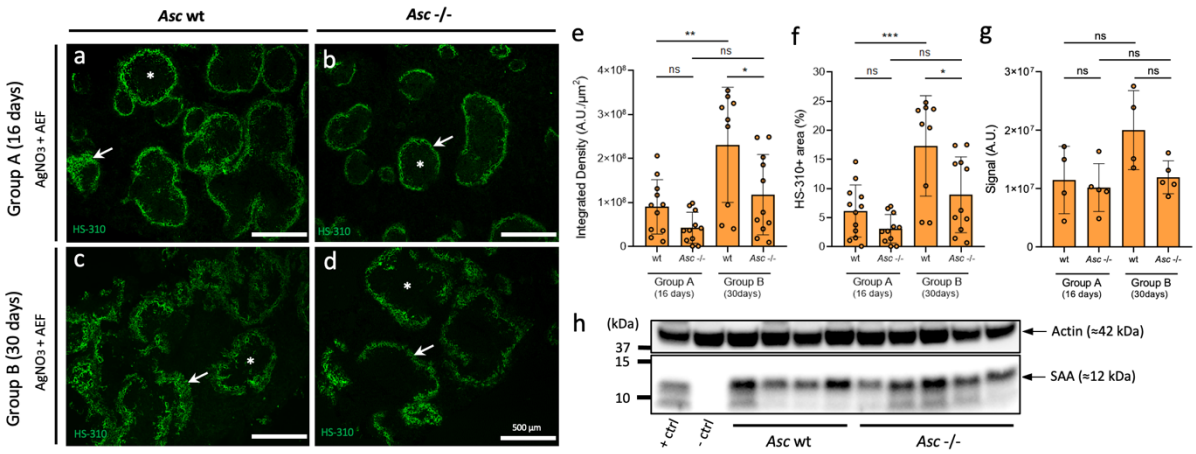

Figure 3.

Decreased splenic amyloid load in the absence of ASC inflammasomes.

Representative LCP-stained spleen sections from AA mice showing amyloid deposits (green) **(a-d)**. *Asc* wt and *Asc*$^{-/-}$ specimen were obtained from groups A and B. *Asc* wt mice exhibited a more pronounced red pulp invasion than the *Asc*$^{-/-}$ mice (white arrows). **(e-f)** Integrated density expressed as arbitrary units/µm^2 (A.U./µm^2) and percentage of HS-310+ area from LCP-stained sections. Each dot represents an individual animal. **(g)** Quantification of SAA western blot given in A.U. **(h)** SAA western blot performed on spleen homogenate from the most intense LCP-stained spleen sections confirms successful AA induction (four from *Asc* wt and five from *Asc*$^{-/-}$). Actin and spleen homogenate from C57BL/6 wt mice served as positive and negative control, respectively. Each dot represents an individual animal. White asterisks (*) represent the white pulp. Spleen sections shown here are representative for respective experimental group. Results shown in scatter plots are represented as mean ± standard deviation (error bars). * $p<0.05$, ** $p<0.01$, *** $p<0.001$, ns; not significant. Post-hoc corrected (Tukey) ANOVA was performed. Scale bars: 500 µm.

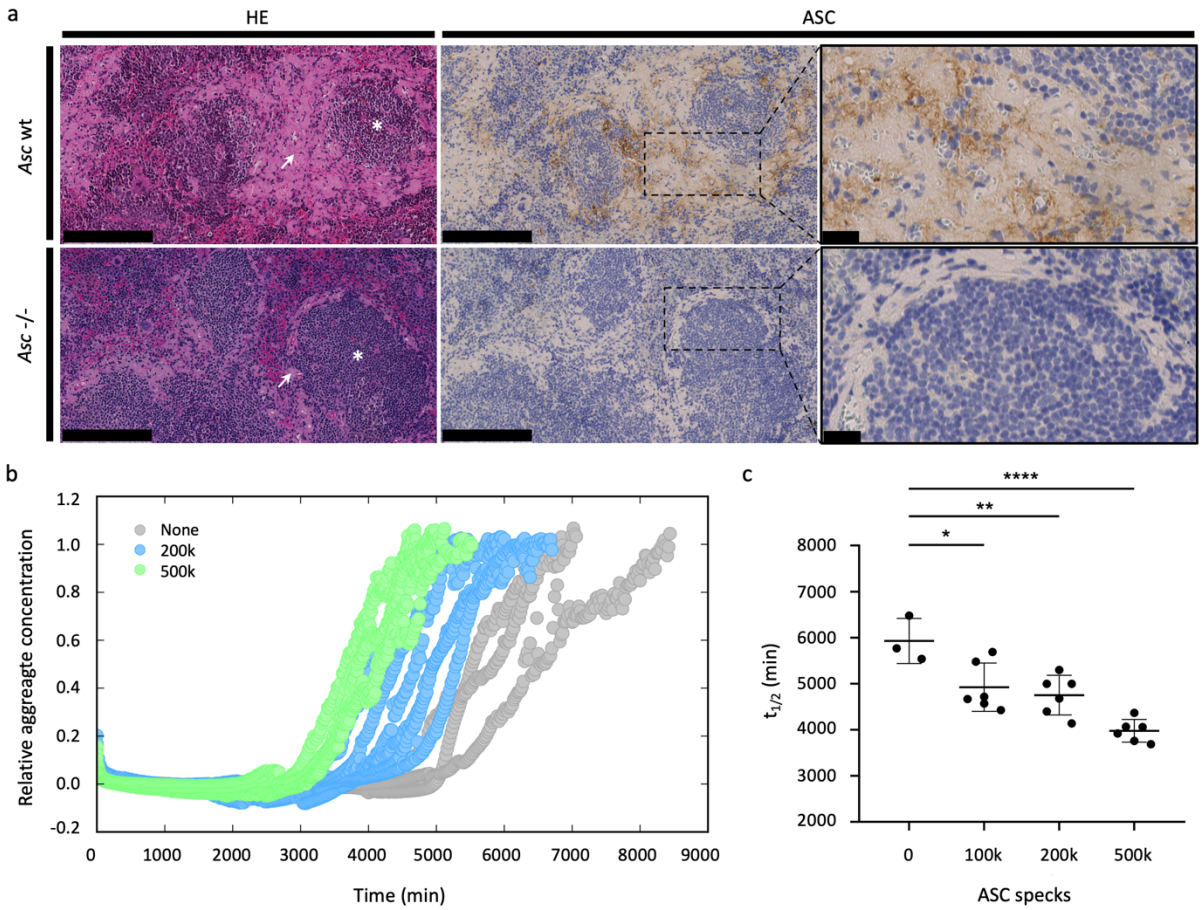

583

584 Figure 4.

585 **ASC is incorporated in splenic amyloid deposits and its presence facilitates and accelerates**
586 **SAA fibril formation in *vitro*.**

587 **(a)** HE staining (left panels) and ASC IHC (middle and right panels) of representative spleen
588 sections from *Asc* wt and *Asc*$^{-/-}$ AA mice. In HE, amyloid appears pink (white arrows). In IHC,
589 ASC appears brown. Sections within boxes (middle panels) are enlarged in the right panels.
590 White asterisks (*) represent the white pulp. Scale bars: 200 µm and 25 µm. **(b)** Relative
591 aggregation concentration of replicates is plotted over time. Replicates that contained murine
592 SAA only are depicted in grey color whereas replicates containing murine SAA as well as 200k
593 or 500k ASC specks are represented in blue and green color, respectively. Each aggregation
594 curve represents one technical replicate. ASC specks only samples did not yield a signal at all
595 (data not shown). **(c)** Mean halftimes ($t_{1/2}$) are plotted for each individual condition: 0, 100k,
596 200k and 500k ASC specks, respectively. * p<0.05, ** p<0.01, **** p<0.0001. Results are

represented as mean ± standard deviation (error bars). Unpaired, two-tailed Students' t-test was performed. Each dot represents one replicate.

599 **Supplemental figures**

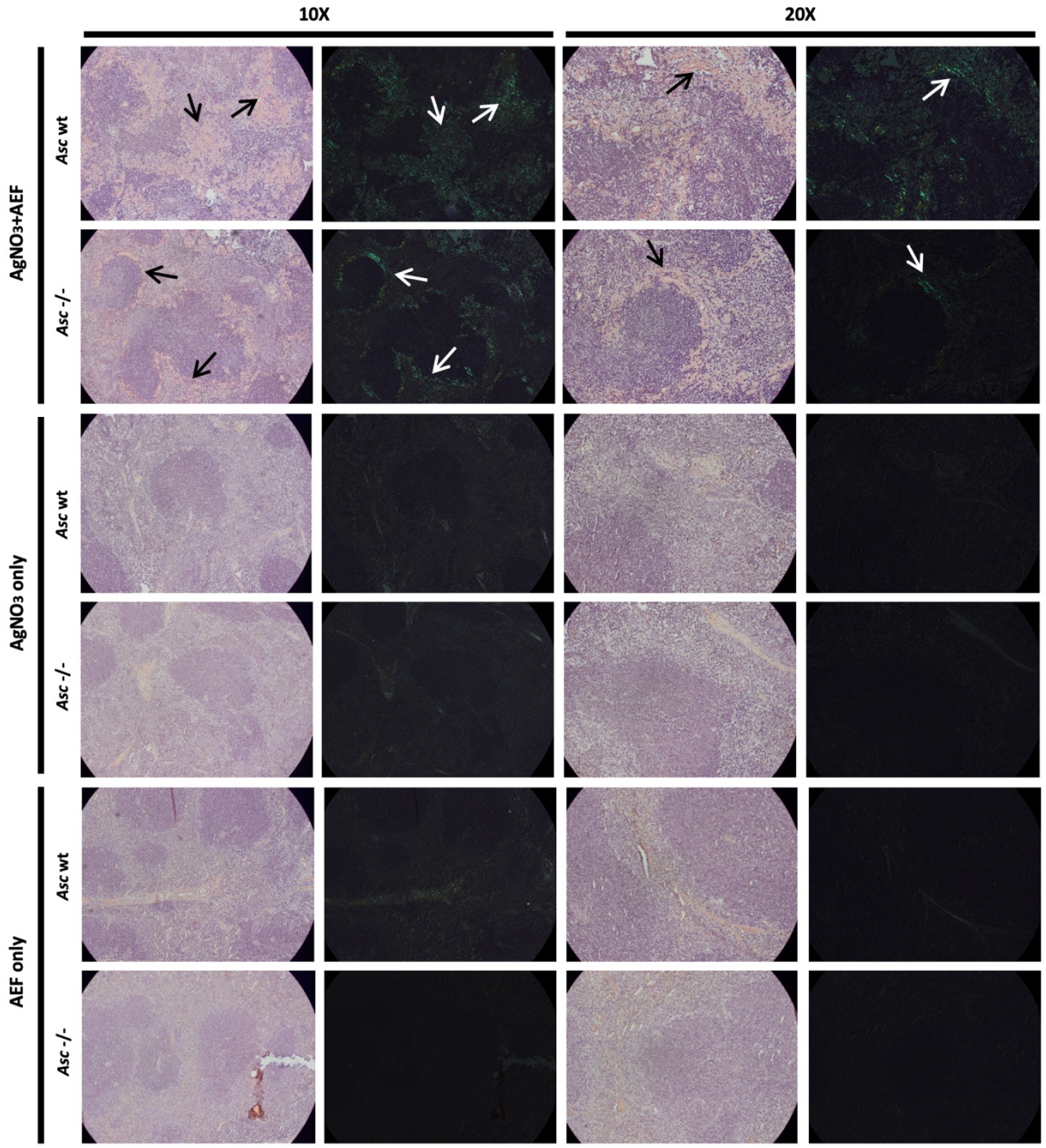

600

601 Figure S1.

602 **Amyloid stained by Congo red shows apple-green birefringence in polarized light only in**
603 **mice with AA induction.**

604 Representative Congo red-stained photo micrographs from indicated experimental groups
605 showing amyloid apple-green birefringence (white arrows) under polarized light in AA mice

606 (64). In light microscopy, amyloid appears as pink amorphous material (black arrows). Of note,
607 there is any amyloid in the AEF-only nor in the AgNO3-only treated group.

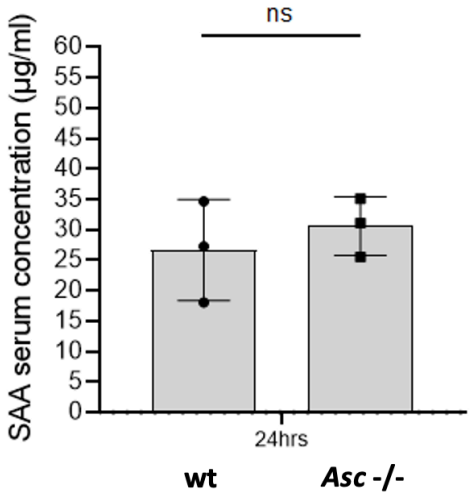

608

609 Figure S2.

610 **Similar peak concentration of Amyloid Enhancing Factor (AEF) in *Asc* wt and *Asc*$^{-/-}$ mice.**

611 Scatter plot depicting SAA levels of AEF-only treated mice at peak concentration 24 hours after
612 AEF injection. No significant difference in SAA serum concentrations (ns) between *Asc* wt and
613 *Asc*$^{-/-}$ mice, suggesting that different *Asc* genotypes did not result in different AEF serum
614 concentrations over time. Each dot represents an individual animal. SAA measurements were
615 performed in technical triplicates. Results are represented as mean ± standard deviation (error
616 bars). ns; not significant. Unpaired, two-tailed Students' t-test was performed. Each dot
617 represents one individual mouse.

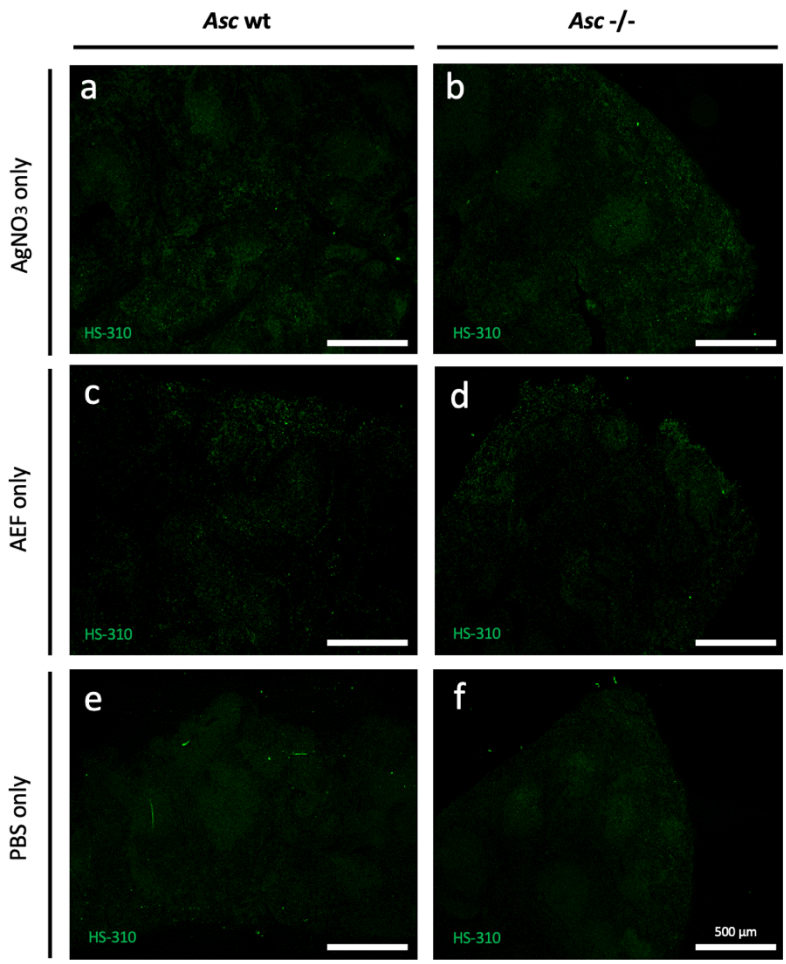

618

619 Figure S3.

620 **Absence of amyloid deposition in mice only treated with $AgNO_3$, AEF or PBS.**

621 Visualization of amyloid deposition by hexameric LCP HS-310. No amyloid was seen in the
622 control groups ($AgNO_3$-only, AEF-only and PBS-only). Light exposure time and 4x microscope
623 objective were kept equal throughout the imaging/experiment.

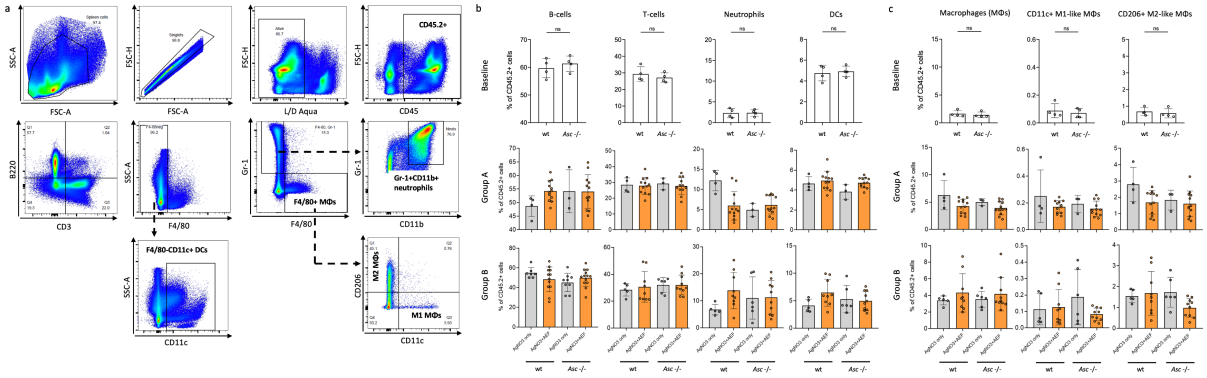

Figure S4.

Assessment of splenic cellular architecture in basal as well as disease state.

(a) Representative flow cytometry analysis and gating strategy of murine spleen cells. CD45.2 is an alloantigen expressed on all hematopoietic cells (except mature erythrocytes and platelets). B cells defined as CD45+CD3-B220+, T cells defined as CD45+B220-CD3+, Dendritic cells (DCs) defined as CD45+F4/80-CD11c+ and Neutrophils defined as CD45+Gr-1+CD11b+. Macrophages (MΦs) defined as CD45+F4/80+, and M1-like MΦs defined as CD45+F4/80+CD206-CD11c+ whereas M2-like MΦs defined as CD45+F4/80+CD11c-CD206+. **(b)** Relative abundance of B cells, T cells, neutrophils and dendritic cells (DCs) are plotted as percentage of CD45.2 positive events. Three different time points are represented. First row of panels: baseline values. Second row of panels: group A (16 days). Third row of panels: group B (30 days). There is no statistically significant difference in splenic cellular composition in unpaired two-tailed Student's t-test between the equivalent experimental group of *Asc* wt and *Asc*$^{-/-}$ mice at each individual time point. Error bar represents standard deviation (SD). Each dot represents an individual mouse. **(c)** F4/80+ macrophages, M1-like MΦs and M2-like MΦs are plotted as percentage of CD45.2 positive events at three different time points. First lane panel represents baseline values whereas data of animals euthanized after 16 days (group A) and 30 days (group B) are plotted in the second and third lane panels, respectively. There was no statistically significant (ns; not significant) difference by unpaired two-tailed Student's t-test in splenic cellular macrophage composition between the equivalent experimental group of *Asc* wt and *Asc*$^{-/-}$ mice at each individual time point. There was no significant difference in the proportion of M1-like MΦs as well as M2-like MΦs (of F4/80+ MΦs) between different

647 time points and genotypes in disease state (data not shown). Results are represented as mean
648 ± standard deviation (error bars). Each dot represents one individual mouse.

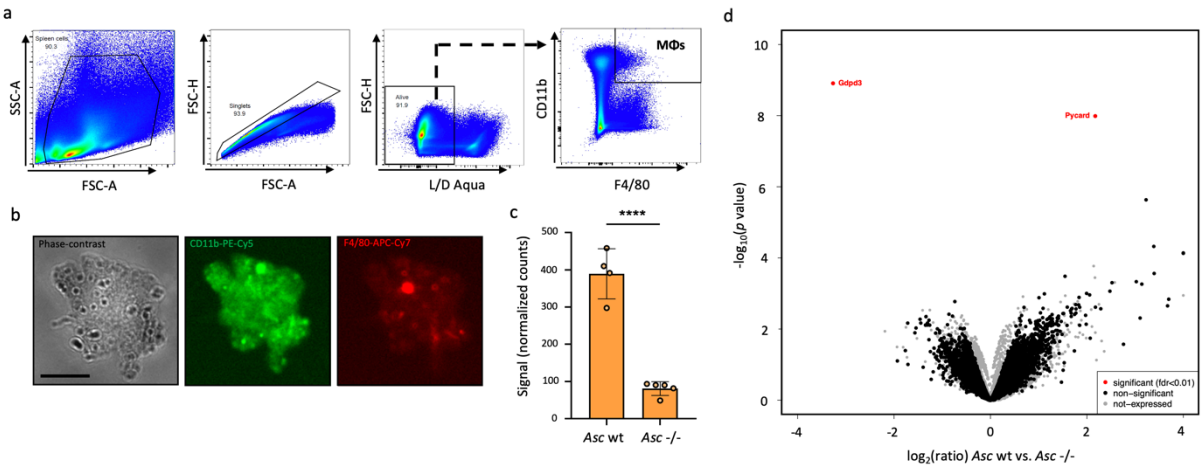

Figure S5.

Transcriptional analysis of splenic macrophages from AA mice reveals mainly changes in *Asc* expression.

(a) Representative gating strategy of splenic macrophages FACS sort from AA mice. Splenic cells were gated first gated in an FSC-A vs. SSC-A plot followed by doublet and dead cell exclusion. Finally, CD11b+F4/80+ macrophages were bulk sorted for transcriptomic analysis. **(b)** To confirm a legit FACS sort, splenic macrophages were assessed using phase contrast and fluorescence microscopy. One can appreciate the amoeboid morphology of a FACS sorted macrophage (left panel). The middle and right panel confirms the presence of the two antibody-conjugated fluorophores PE-Cy5 and APC-Cy7 that were used to identify CD11b+ and F4/80+ macrophages, respectively. Scale bar: approximately 10 µm. **(c)** Scatter plot depicting normalized counts of ASC transcript reads. An unpaired, two-tailed Students' t-tests was performed. **** $p<0.0001$. Each dot represents one individual mouse. **(d)** 'Volcano plot' of statistical significance vs. foldchange between *Asc* wt and *Asc*$^{-/-}$ splenic macrophages from AA mice displays the most significantly and differentially expressed genes (in red).

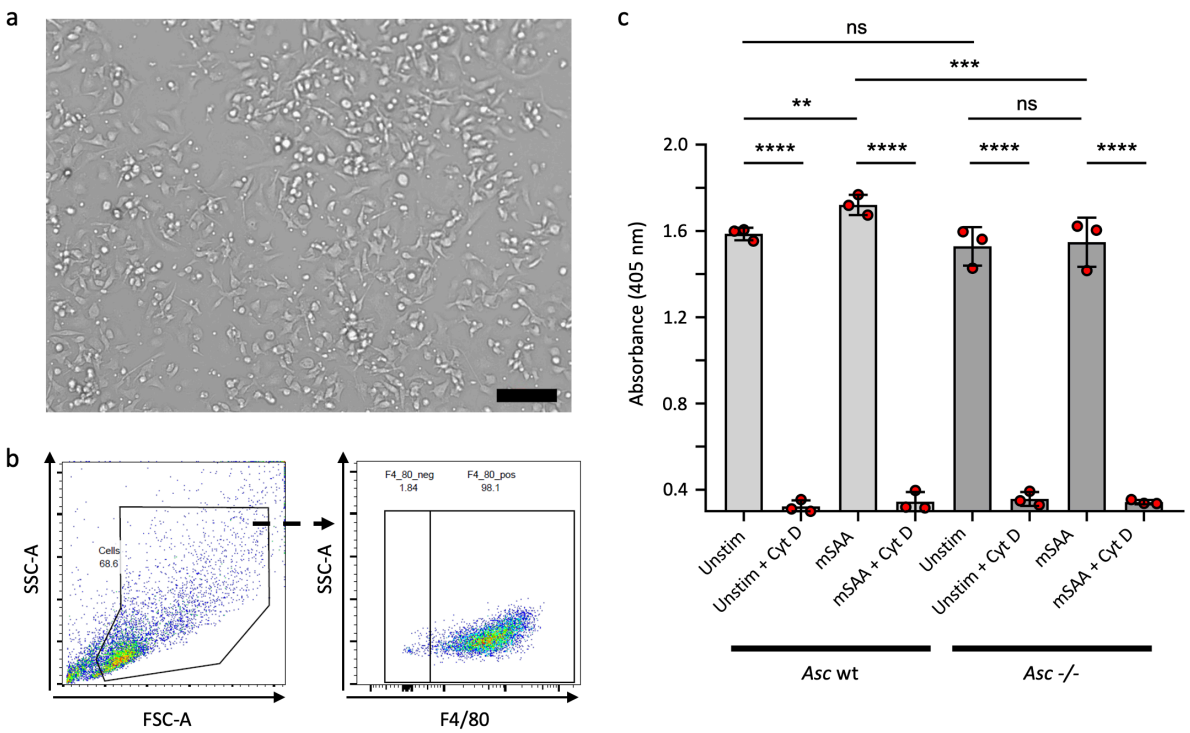

Figure S6.

***In vitro* phagocytosis of SAA-stimulated BMDMs.**

(a) Phase contrast micrograph of adherent and differentiated BMDMs. Scale bar: 100 µm. **(b)** To assess BMDMs differentiation, flow cytometry was performed with anti-mouse F4/80 antibody, a specific macrophage marker. Alive (not shown) F4/80+ cells represent differentiated BMDMs. **(c)** Scatter plots depicting phagocytosis (OD) from unstimulated and mSAA-stimulated *Asc* wt as well as *Asc*-/- BMDMs specimens. Each condition of the assay was carried out in technical duplicates. 10 µM Cytochalasin D phagocytosis inhibitor was used. Results are represented as mean ± standard deviation (error bars). ** $p<0.01$, *** $p<0.001$, **** $p<0.0001$, ns; not significant. Statistics was performed using a two-way post hoc adjusted ANOVA and unpaired, two-tailed Students' t-tests. Each dot represents one individual bone marrow.

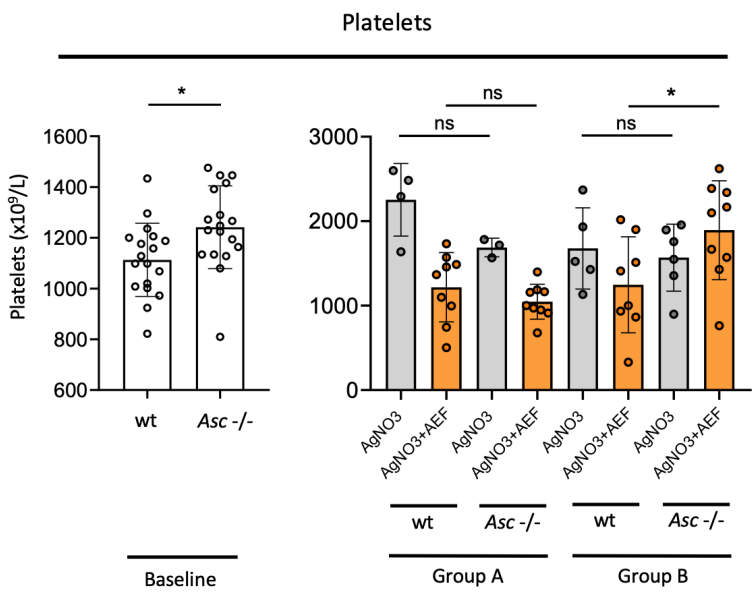

678

679 Figure S7.

680 **Altered platelet count in baseline as well as disease state in the absence of ASC.**

681 Scatter plots depicting platelet counts from experimental mice and different time points are
682 represented. Results are represented as mean ± standard deviation (error bars). *Asc*$^{-/-}$ mice
683 showed increased platelet counts at baseline, as did AA mice from group B. There was no
684 significant (ns) difference between $AgNO_3$-only treatment or AA induced mice of group A nor
685 in $AgNO_3$-only treated group in group B. Platelet counts < 150 x10^9/L were excluded from
686 analysis. * p<0.05, ns; not significant. Analysis was performed using unpaired two-tailed
687 Students' t-tests. Each dot represents one individual mouse.

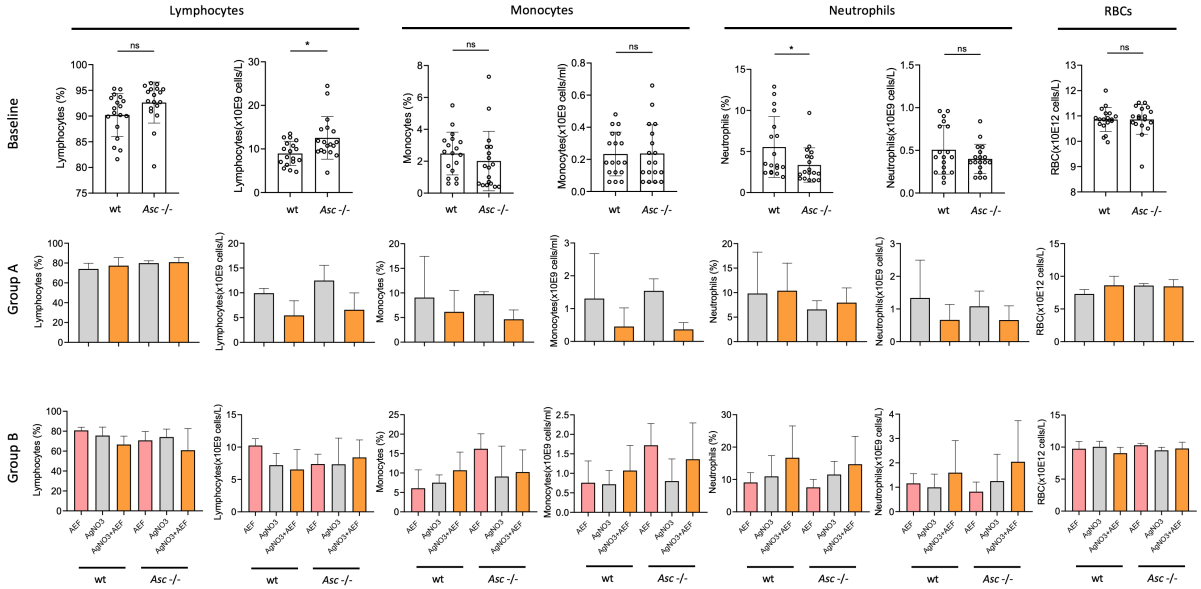

Figure S8.

Assessment of complete blood count (CBC) in basal and disease state.

Scatter plots depicting the abundance of lymphocytes, monocytes, neutrophils red blood cells (RBCs) plotted in relative (%) as well as absolute values (cell numbers). First lane panel represents baseline values of *Asc* wt and *Asc*$^{-/-}$ mice. Data of mice euthanized at day 16 (group A) and day 30 (group B) are plotted in the second and third lane panels, respectively. There was no significant difference between equivalent experimental groups of same genotype in basal as well as disease state. Results are represented as mean ± standard deviation (error bars). * $p<0.05$, ns; not significant. Statistical analysis performed by unpaired two-tailed Student's t-test in CBC between the equivalent experimental group. Each dot represents one individual mouse.

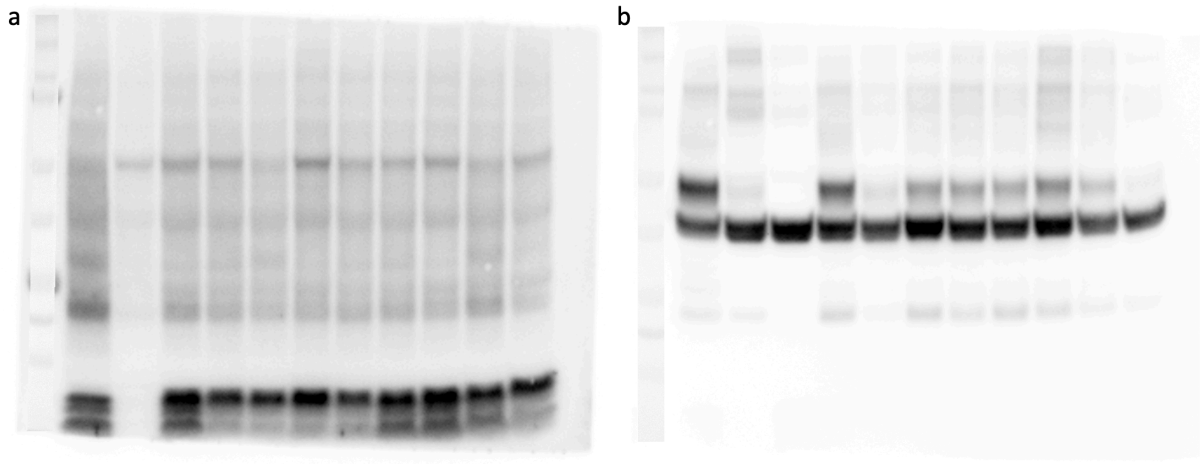

Figure S9.

Uncropped and unmodified western blot images of Figure 3.

(a) Uncropped image of western blot that was performed on spleen homogenate of AA mice and probed with anti-SAA primary antibody for SAA detection. **(b)** Uncropped image of western blot that was performed on spleen homogenate of AA mice and probed with anti-Actin primary antibody (loading control).

707 **Supplemental tables**

708

709 Table S1. **Genotype and sex of experimental animals.**

710

Group / Gender	AEF+$AgNO_3$ Group A and B	$AgNO_3$ only Group A and B	PBS only	AEF only	Total (n =)
***Asc*$^{-/-}$** females (n =)	10	4	3	1	18
***Asc*$^{-/-}$** males (n =)	14	6	0	3	23
***Asc* wt** females (n =)	10	4	0	0	14
***Asc* wt** males (n =)	12	6	3	3	24
Total (n =)	46	20	6	7	79

711

712

713 Table S2. **Genotype and age of experimental animals.**

714

Genotype / Group	*Asc* wt	*Asc*$^{-/-}$	*p*-value	Sign.
PBS-only (mean days ± SD)	77.67 ± 1.16	58.33 ± 19.63	0.164	ns
AEF-only (mean days ± SD)	80.33 ± 1.16	59.75 ± 15.17	0.071	ns
$AgNO_3$-only (mean days ± SD)	100.0 ± 20.07	94.8 ± 21.14	0.580	ns
$AgNO_3$ + AEF (mean days ± SD)	81.68 ± 12.11	88.96 ± 16.53	0.101	ns
Total (mean days ± SD)	86.08 ± 15.93	85.20 ± 21.18	0.837	ns

715

716

717 Table S3. **Temporal SAA serum concentrations upon silver nitrate injection or AA induction.**

718

	Asc wt		*Asc*$^{-/-}$	
Group / Time (hrs)	$AgNO_3$ Mean ± SD (µg/ml)	$AgNO_3$+AEF Mean ± SD (µg/ml)	$AgNO_3$ Mean ± SD (µg/ml)	$AgNO_3$+AEF Mean ± SD (µg/ml)
Baseline	6.08 ± 6.44	1.49 ± 1.22	1.39 ± 0.99	1.27 ± 1.06
9h	84.44 ± 15.22	63.41 ± 36.12	49.08 ± 38.48	80.98 ± 49.2
24h	217.1 ± 124.5	125.4 ± 25.04	188.5 ± 120	231.9 ± 97.13
48h	118 ± 60.21	95.2 ± 40.01	106.5 ± 65.24	149 ± 34.62
72h	19.22 ± 10.65	16 ± 5.94	16.16 ± 7.7	26.69 ± 10.79
96h	3.28 ± 0.47	3.48 ± 1.55	4.38 ± 0.79	7.04 ± 5.77

719

720

721 Table S4. **HS-310-stained AA amyloid.**

722

	Asc wt		*Asc*$^{-/-}$	
Group / Time (days)	$AgNO_3$ Mean ± SD (HS-310 area, %)	$AgNO_3$+AEF Mean ± SD (HS-310 area, %)	$AgNO_3$ Mean ± SD (HS-310 area, %)	$AgNO_3$+AEF Mean ± SD (HS-310 area, %)
Group A	-	6.13 ± 4.48	-	3.10 ± 2.46
Group B	-	17.33 ± 8.60	-	8.39 ± 6.5

723

724

725 Table S5. **Accelerated SAA fibrillation in the presence of ASC specks.**

726

ASC specks (abs) / Time ($t_{1/2}$)	0	1 x 10^5	2 x 10^5	5 x 10^5
Mean ± SD (hours)	98.83 ± 8.16	82.12 ± 8.73	79.22 ± 7.18	66.30 ± 4.10

727

728

729 Table S6. **Phagocytosis of *Asc* wt and *Asc*$^{-/-}$ BMDMs.**

730

Genotype / Condition BMDMs	*Asc* wt Mean ± SD OD at 405 nm	Asc$^{-/-}$ Mean ± SD OD at 405 nm	*p*-value	Sign.
Unstimulated	1.58 ± 0.03	1.53 ± 0.09	0.194	ns
Unstimulated + Cytochalasin D	0.32 ± 0.03	0.35 ± 0.03	0.167	ns
mSAA stimulated	1.72 ± 0.05	1.55 ± 0.11	0.0002	sign.
mSAA stimulated + Cytochalasin D	0.34 ± 0.05	0.34 ± 0.01	0.999	ns

731

732

733 **Supplemental material and methods tables**

734

735 Table S7. **Western blot antibodies.**

736

Antibody	Clone	Host / Conjugate	Source	Dilution (µl)
SAA recombinant rabbit monoclonal	D9H4L41	Rabbit	Invitrogen, #700830	1:200
Goat anti-rabbit IgG (H+L)	-	Goat/ HRP	Jackson Immuno, #111-035-045	1:5000
Anti-Actin Antibody monoclonal	C4	Mouse	Merck, #MAB1501R	1:8000
Goat anti-mouse IgG (H+L)	-	Goat/ HRP	Jackson Immuno, #115-035-003	1:8000

737

738

739 Table S8. **Flow cytometry antibodies.**

740

Surface antigen	Fluorophore	Source	Dilution (µl)
Anti-mouse B220	Brilliant Violet 785	Biolegend, #103245	1:400
Anti-mouse CD11b	Brilliant Violet 650	Biolegend, #101239	1:400
Anti-mouse CD45.2	Pacific Blue	Biolegend, #109820	1:100
Anti-mouse CD3	Per/CPCy5.5	Biolegend, #100218	1:100
Anti-mouse Gr-1	PE/Cy5	eBioscience™, #15-5931-82	1:400
Anti-mouse CD206	PE	Biolegend, #141705	1:100
Anti-mouse F4/80	APC-eFluor 780	eBioscience™, #47-4801-82	1:200
Anti-mouse MHCII	Alexa Fluor® 700	Biolegend, #107621	1:800
Anti-mouse CD11c	APC	eBioscience™, #17-0114-82	1:400

741

742

References

1. Sack GH. Serum amyloid A - a review. *Mol Med.* 2018;24(1):46.
2. Ye RD, and Sun L. Emerging functions of serum amyloid A in inflammation. *J Leukoc Biol.* 2015;98(6):923-9.
3. Röcken C, and Shakespeare A. Pathology, diagnosis and pathogenesis of AA amyloidosis. *Virchows Arch.* 2002;440(2):111-22.
4. Liberta F, Loerch S, Rennegarbe M, Schierhorn A, Westermark P, Westermark GT, et al. Cryo-EM fibril structures from systemic AA amyloidosis reveal the species complementarity of pathological amyloids. *Nat Commun.* 2019;10(1):1104.
5. Simons JP, Al-Shawi R, Ellmerich S, Speck I, Aslam S, Hutchinson WL, et al. Pathogenetic mechanisms of amyloid A amyloidosis. *Proc Natl Acad Sci U S A.* 2013;110(40):16115-20.
6. Sun L, and Ye RD. Serum amyloid A1: Structure, function and gene polymorphism. *Gene.* 2016;583(1):48-57.
7. Tape C, Tan R, Nesheim M, and Kisilevsky R. Direct evidence for circulating apoSAA as the precursor of tissue AA amyloid deposits. *Scand J Immunol.* 1988;28(3):317-24.
8. Prelli F, Pras M, and Frangione B. Degradation and deposition of amyloid AA fibrils are tissue specific. *Biochemistry.* 1987;26(25):8251-6.
9. Liepnieks JJ, Kluve-Beckerman B, and Benson MD. Characterization of amyloid A protein in human secondary amyloidosis: the predominant deposition of serum amyloid A1. *Biochim Biophys Acta.* 1995;1270(1):81-6.
10. Westermark GT, and Westermark P. Serum amyloid A and protein AA: molecular mechanisms of a transmissible amyloidosis. *FEBS Lett.* 2009;583(16):2685-90.
11. Papa R, and Lachmann HJ. Secondary, AA, Amyloidosis. *Rheum Dis Clin North Am.* 2018;44(4):585-603.
12. Brunger AF, Nienhuis HLA, Bijzet J, and Hazenberg BPC. Causes of AA amyloidosis: a systematic review. *Amyloid.* 2020;27(1):1-12.
13. Westermark GT, Fändrich M, and Westermark P. AA amyloidosis: pathogenesis and targeted therapy. *Annu Rev Pathol.* 2015;10:321-44.
14. Lamkanfi M, and Dixit VM. Mechanisms and functions of inflammasomes. *Cell.* 2014;157(5):1013-22.
15. Heneka MT, Kummer MP, and Latz E. Innate immune activation in neurodegenerative disease. *Nat Rev Immunol.* 2014;14(7):463-77.
16. Heneka MT, Golenbock DT, and Latz E. Innate immunity in Alzheimer's disease. *Nat Immunol.* 2015;16(3):229-36.
17. Anders HJ, and Muruve DA. The inflammasomes in kidney disease. *J Am Soc Nephrol.* 2011;22(6):1007-18.
18. Fernandes-Alnemri T, Wu J, Yu JW, Datta P, Miller B, Jankowski W, et al. The pyroptosome: a supramolecular assembly of ASC dimers mediating inflammatory cell death via caspase-1 activation. *Cell Death Differ.* 2007;14(9):1590-604.
19. Franklin BS, Bossaller L, De Nardo D, Ratter JM, Stutz A, Engels G, et al. The adaptor ASC has extracellular and 'prionoid' activities that propagate inflammation. *Nat Immunol.* 2014;15(8):727-37.
20. Lu A, Magupalli VG, Ruan J, Yin Q, Atianand MK, Vos MR, et al. Unified polymerization mechanism for the assembly of ASC-dependent inflammasomes. *Cell.* 2014;156(6):1193-206.
21. Redondo-Castro E, Faust D, Fox S, Baldwin AG, Osborne S, Haley MJ, et al. Development of a characterised tool kit for the interrogation of NLRP3 inflammasome-dependent responses. *Sci Rep.* 2018;8(1):5667.
22. Agrawal I, and Jha S. Comprehensive review of ASC structure and function in immune homeostasis and disease. *Mol Biol Rep.* 2020;47(4):3077-96.
23. Hauenstein AV, Zhang L, and Wu H. The hierarchical structural architecture of inflammasomes, supramolecular inflammatory machines. *Curr Opin Struct Biol.* 2015;31:75-83.
24. Ising C, Venegas C, Zhang S, Scheiblich H, Schmidt SV, Vieira-Saecker A, et al. NLRP3 inflammasome activation drives tau pathology. *Nature.* 2019;575(7784):669-73.
25. Venegas C, Kumar S, Franklin BS, Dierkes T, Brinkschulte R, Tejera D, et al. Microglia-derived ASC specks cross-seed amyloid-β in Alzheimer's disease. *Nature.* 2017;552(7685):355-61.
26. Dansokho C, and Heneka MT. Neuroinflammatory responses in Alzheimer's disease. *J Neural Transm (Vienna).* 2018;125(5):771-9.

27. Fernandes-Alnemri T, and Alnemri ES. Assembly, purification, and assay of the activity of the ASC pyroptosome. *Methods Enzymol.* 2008;442:251-70.
28. Balci-Peynircioglu B, Waite AL, Schaner P, Taskiran ZE, Richards N, Orhan D, et al. Expression of ASC in renal tissues of familial mediterranean fever patients with amyloidosis: postulating a role for ASC in AA type amyloid deposition. *Exp Biol Med (Maywood).* 2008;233(11):1324-33.
29. Niemi K, Teirilä L, Lappalainen J, Rajamäki K, Baumann MH, Öörni K, et al. Serum amyloid A activates the NLRP3 inflammasome via P2X7 receptor and a cathepsin B-sensitive pathway. *J Immunol.* 2011;186(11):6119-28.
30. Chen W, Qiang X, Wang Y, Zhu S, Li J, Babaev A, et al. Identification of tetranectin-targeting monoclonal antibodies to treat potentially lethal sepsis. *Sci Transl Med.* 2020;12(539).
31. Lundmark K, Vahdat Shariatpanahi A, and Westermark GT. Depletion of spleen macrophages delays AA amyloid development: a study performed in the rapid mouse model of AA amyloidosis. *PLoS One.* 2013;8(11):e79104.
32. Sponarova J, Nuvolone M, Whicher C, Frei N, Kana V, Schwarz P, et al. Efficient amyloid A clearance in the absence of immunoglobulins and complement factors. *Am J Pathol.* 2013;182(4):1297-307.
33. Kisilevsky R, and Boudreau L. Kinetics of amyloid deposition. I. The effects of amyloid-enhancing factor and splenectomy. *Lab Invest.* 1983;48(1):53-9.
34. Magy N, Liepnieks JJ, Benson MD, and Kluve-Beckerman B. Amyloid-enhancing factor mediates amyloid formation on fibroblasts via a nidus/template mechanism. *Arthritis Rheum.* 2003;48(5):1430-7.
35. Kennel SJ, Macy S, Wooliver C, Huang Y, Richey T, Heidel E, et al. Phagocyte depletion inhibits AA amyloid accumulation in AEF-induced huIL-6 transgenic mice. *Amyloid.* 2014;21(1):45-53.
36. Nyström SN, and Westermark GT. AA-Amyloid is cleared by endogenous immunological mechanisms. *Amyloid.* 2012;19(3):138-45.
37. Gabay C, and Kushner I. Acute-phase proteins and other systemic responses to inflammation. *N Engl J Med.* 1999;340(6):448-54.
38. Eisenbarth SC, Colegio OR, O'Connor W, Sutterwala FS, and Flavell RA. Crucial role for the Nalp3 inflammasome in the immunostimulatory properties of aluminium adjuvants. *Nature.* 2008;453(7198):1122-6.
39. Vahdat Shariat Panahi A, Hultman P, Öllinger K, Westermark GT, and Lundmark K. Lipid membranes accelerate amyloid formation in the mouse model of AA amyloidosis. *Amyloid.* 2019;26(1):34-44.
40. Erdem E, Erdem D, Dilek M, Kaya C, Karataş A, Kut E, et al. Red cell distribution width and mean platelet volume in amyloidosis. *Clin Appl Thromb Hemost.* 2014;20(3):334-7.
41. Bakan A, Oral A, Alışır Ecder S, Şaşak Kuzgun G, Elçioğlu Ö, Demirci R, et al. Assessment of Mean Platelet Volume in Patients with AA Amyloidosis and AA Amyloidosis Secondary to Familial Mediterranean Fever: A Retrospective Chart - Review Study. *Med Sci Monit.* 2019;25:3854-9.
42. Rolfes V, Ribeiro LS, Hawwari I, Böttcher L, Rosero N, Maasewerd S, et al. Platelets Fuel the Inflammasome Activation of Innate Immune Cells. *Cell Rep.* 2020;31(6):107615.
43. Sponarova J, Nyström SN, and Westermark GT. AA-amyloidosis can be transferred by peripheral blood monocytes. *PLoS One.* 2008;3(10):e3308.
44. Couturier J, Stancu IC, Schakman O, Pierrot N, Huaux F, Kienlen-Campard P, et al. Activation of phagocytic activity in astrocytes by reduced expression of the inflammasome component ASC and its implication in a mouse model of Alzheimer disease. *J Neuroinflammation.* 2016;13:20.
45. Mariathasan S, Newton K, Monack DM, Vucic D, French DM, Lee WP, et al. Differential activation of the inflammasome by caspase-1 adaptors ASC and Ipaf. *Nature.* 2004;430(6996):213-8.
46. Lammert CR, Frost EL, Bellinger CE, Bolte AC, McKee CA, Hurt ME, et al. AIM2 inflammasome surveillance of DNA damage shapes neurodevelopment. *Nature.* 2020;580(7805):647-52.
47. Nuvolone M, and Merlini G. Systemic amyloidosis: novel therapies and role of biomarkers. *Nephrol Dial Transplant.* 2017;32(5):770-80.
48. Gellermann GP, Appel TR, Tannert A, Radestock A, Hortschansky P, Schroeckh V, et al. Raft lipids as common components of human extracellular amyloid fibrils. *Proc Natl Acad Sci U S A.* 2005;102(18):6297-302.
49. Röcken C, Menard R, Bühling F, Vöckler S, Raynes J, Stix B, et al. Proteolysis of serum amyloid A and AA amyloid proteins by cysteine proteases: cathepsin B generates AA amyloid proteins and cathepsin L may prevent their formation. *Ann Rheum Dis.* 2005;64(6):808-15.

50. Richards DB, Cookson LM, Barton SV, Liefaard L, Lane T, Hutt DF, et al. Repeat doses of antibody to serum amyloid P component clear amyloid deposits in patients with systemic amyloidosis. *Sci Transl Med.* 2018;10(422).
51. Magy N, Benson MD, Liepnieks JJ, and Kluve-Beckerman B. Cellular events associated with the initial phase of AA amyloidogenesis: insights from a human monocyte model. *Amyloid.* 2007;14(1):51-63.
52. Kluve-Beckerman B, Manaloor JJ, and Liepnieks JJ. A pulse-chase study tracking the conversion of macrophage-endocytosed serum amyloid A into extracellular amyloid. *Arthritis Rheum.* 2002;46(7):1905-13.
53. Lundmark K, Westermark GT, Nystrom S, Murphy CL, Solomon A, and Westermark P. Transmissibility of systemic amyloidosis by a prion-like mechanism. *Proc Natl Acad Sci U S A.* 2002;99(10):6979-84.
54. Nilsson KP, Ikenberg K, Aslund A, Fransson S, Konradsson P, Röcken C, et al. Structural typing of systemic amyloidoses by luminescent-conjugated polymer spectroscopy. *Am J Pathol.* 2010;176(2):563-74.
55. Sjölander D, Röcken C, Westermark P, Westermark GT, Nilsson KP, and Hammarström P. Establishing the fluorescent amyloid ligand h-FTAA for studying human tissues with systemic and localized amyloid. *Amyloid.* 2016;23(2):98-108.
56. Wahlström N, Edlund U, Pavia H, Toth G, Jaworski A, Pell AJ, et al. Cellulose from the green macroalgae Ulva lactuca: isolation, characterization, optotracing, and production of cellulose nanofibrils.
57. Claus S, Meinhardt K, Aumüller T, Puscalau-Girtu I, Linder J, Haupt C, et al. Cellular mechanism of fibril formation from serum amyloid A1 protein. *EMBO Rep.* 2017;18(8):1352-66.
58. Martín-Sánchez F, Gómez AI, and Pelegrín P. Isolation of Particles of Recombinant ASC and NLRP3. *Bio Protoc.* 2015;5(10).
59. Meisl G, Kirkegaard JB, Arosio P, Michaels TC, Vendruscolo M, Dobson CM, et al. Molecular mechanisms of protein aggregation from global fitting of kinetic models. *Nat Protoc.* 2016;11(2):252-72.
60. Yanagita T, Murata Y, Tanaka D, Motegi SI, Arai E, Daniwijaya EW, et al. Anti-SIRP. *JCI Insight.* 2017;2(1):e89140.
61. Ono Y, Nagai M, Yoshino O, Koga K, Nawaz A, Hatta H, et al. CD11c+ M1-like macrophages (MΦs) but not CD206+ M2-like MΦ are involved in folliculogenesis in mice ovary. *Sci Rep.* 2018;8(1):8171.
62. Arlt A, von Bonin F, Rehberg T, Perez-Rubio P, Engelmann JC, Limm K, et al. High CD206 levels in Hodgkin lymphoma-educated macrophages are linked to matrix-remodeling and lymphoma dissemination. *Mol Oncol.* 2020;14(3):571-89.
63. Nawaz A, Aminuddin A, Kado T, Takikawa A, Yamamoto S, Tsuneyama K, et al. CD206. *Nat Commun.* 2017;8(1):286.
64. Jagusiak A, Rybarska J, Konieczny L, Piekarska B, Stopa B, Chłopaś K, et al. Amyloids, Congo red and the apple-green effect. *Acta Biochim Pol.* 2019;66(1):39-46.